Effect of Nd and Mn Co-Doping on Dielectric, Ferroelectric and Photovoltaic Properties of BiFeO$_3$

Qiyuan Wu [1], Yanling Song [1], Caihong Jia [1], Zhaomeng Gao [2] and Weifeng Zhang [1,*]

1   Key Laboratory of Photovoltaic Materials, Center for Topological Functional Materials, Henan University, Kaifeng 475004, China; 104754190994@henu.edu.cn (Q.W.); songyl712@163.com (Y.S.); chjia@henu.edu.cn (C.J.)
2   Key Laboratory of Polar Materials and Devices (MOE), Department of Electronics, East China Normal University, Shanghai 200241, China; zm_gaojx@163.com
*   Correspondence: wfzhang@henu.edu.cn

Abstract: Bi$_{1-x}$Nd$_x$Fe$_{0.99}$Mn$_{0.01}$O$_3$ (BNFMO, x = 0.00~0.20) films were epitaxially grown on Nb:SrTiO$_3$ (001) substrates using pulsed laser deposition. It was found that the Nd-doping concentration has a great impact on the surface morphology, crystal structure, and electrical properties. BNFMO thin film with low Nd-doping concentration (≤16%) crystallizes into a rhombohedral structure, while the high Nd-doping (>16%) will lead to the formation of an orthogonal structure. Furthermore, to eliminate the resistive switching (RS) effect, a positive-up–negative-down (PUND) measurement was applied on two devices in series. The remnant polarization experiences an increase with the Nd-doping concentration increasing to 16%, then drops down with the further increased concentration of Nd. Finally, the ferroelectric photovoltaic effect is also regulated by the ferroelectric polarization, and the maximum photocurrent of 1758 μA/cm^2 was obtained in Bi$_{0.84}$Nd$_{0.16}$Fe$_{0.99}$Mn$_{0.01}$O$_3$ thin film. BNFMO films show great potential for ferroelectric and photovoltaic applications.

Keywords: BiFeO$_3$ film; piezoresponse force microscopy; dielectric; PUND measurement; ferroelectric; photovoltaic

1. Introduction

BiFeO$_3$ (BFO), one of the few multiferroic materials with antiferromagnetic, ferroelectricity, and ferroelectric photovoltaic responses at room temperature, has captured much attention [1–3]. Moreover, the low cost and simple fabrication approach of flexible BFO films can also be utilized in wearable hybrid piezoelectric–triboelectric nanogenerators H-P/TENG [4–7]. To grow BFO thin films, high substrate temperature during growth is needed for physical or chemical methods. During annealing, the volatilization of Bi^{3+} will produce oxygen vacancy content and transform Fe^{3+} to Fe^{2+} due to the charge compensation, which will lead to the weak ferroelectric properties of the sample [8]. Thus, it is generally difficult to obtain relatively regular ferroelectric polarization hysteresis (polarization voltage, *P–V*) loops in BFO films. In recent years, in order to enhance the properties of BFO, doping is widely adopted [9–14]. Additionally, research on BFO thin films, co-doped by Nd and transition metal elements, has been frequently reported [15–20]. Despite this, there has been little research completed on eliminating the effects of leakage current during ferroelectric polarization hysteresis measurements of BFO films. For example, the Nd and Mn co-doped BFO epitaxial film prepared by Kawae et al. [19,21] and the Nd-doped BFO films manufactured by Xue et al. [16] with large ferroelectric polarization cannot obtain the real properties of ferroelectric polarization due to the severe leakage of the current. Thereby, not only does the technology of thin film preparation need to be enhanced, but more advanced measurement methods to eliminate the effect of environment and the leakage of current are also required when attempting to promote the ferroelectric properties of BFO films by using the approach of ion-doping substitution. Moreover, the photovoltaic

effect of BFO also attracted the attention of researchers [22–24] and doping is often adopted to increase the photovoltaic effect. Mn-doping of BFO prepared by Nakashima et al. [25] enhanced the photovoltage. In a Pt/Mn 1 at%-doped BFO/Pt coplanar capacitor with an inter-electrode distance of 260 μm, V_{OC} reached 280 V at room temperature (RT) (852 V at 80 K). An approach, 'gap-state' engineering, has been developed to produce photoferroelectrics of Mn-BFO film reported by Matsuo et al. [26], in which defect states within the bandgap act as a scaffold for photogeneration. The tunable and low bandgap Bi_2FeCrO_6 (BFCO) thin films were engineered by Nechache et al. [27] with an unprecedented power conversion efficiency of 8.1%. Gupta et al. [28] reported the superior photovoltaic property in $BiFe_{0.95}Si_{0.05}O_3$ films with high photosensitivity $V_{OC} \sim 0.45$ V and $I_{SC} \sim 0.75$ mA.

The photocurrent is one of the important factors for judging the merits of the photovoltaic effect. Qin et al. [29–31] reported that PLZT thin films generally have an optimal thickness peak with the maximum photocurrent, and the range of the peak is around 30–40 nm. In addition, the crystal structure of polycrystalline film has more defects, reducing the lifetime of photo-generated carriers. However, the sample preparations of ion-doped BFO films reported in previous work are relatively thick and mostly polycrystalline films. For example, the thickness of Nd-doped and Nd-Cr co-doped BFO polycrystalline films prepared by Shi et al. [32] and Zhang et al. [33] are thick and the dielectric permittivity of the selected Ag electrode is small. According to previous reports [29], the selection of electrodes is also an important factor that affects the photocurrent of ferroelectric films. Additionally, the thickness of Nd-doped BFO single crystal films prepared by Tan et al. [34] is too thick, while the La-doped BFO polycrystalline films prepared by Biswas et al. [35] have poor quality. Thus, achieving a reliable ferroelectric polarization hysteresis loop and enhancing the photovoltaic response of BFO films becomes important.

We summarize related studies on ion-doping of BFO films and identify the strengths and weaknesses of each. In addition, previous reports have not proposed the influence of Nd and Mn co-doping on ferroelectric photovoltaic properties of BFO thin films. Thus, in this paper, five ratios were selected to study the effect of Nd ion-doping on the morphology, structure, dielectric, ferroelectric, and photovoltaic properties of $BiFe_{0.99}Mn_{0.01}O_3$ film in detail. Additionally, 1 at% Mn^{4+}-doping on the Fe-site is adopted to optimize the ferroelectric properties. For BFO materials, the ion substitutions with a high valence (4+) for the Fe site usually result in the decrease in oxygen vacancy content and the increase in Fe^{2+} [36,37] ($Bi_{1-x}Nd_xFe_{0.99}Mn_{0.01}O_3$, x = 0.00, 0.05, 0.10, 0.16, 0.20, BNFMO). The 40-nm-thick epitaxial BNFMO films with high quality and no impurity phase were prepared on NSTO. The structure of two devices in series was utilized for *P–V* loop measurements of BNFMO films during the positive-up–negative-down (PUND) measurement, and successfully deducting the influence of leakage current, resistive switching (RS) effect, and environmental factors. In addition, we obtained the maximum photocurrent of 1758 μA/cm^2 in $Bi_{0.84}Nd_{0.16}Fe_{0.99}Mn_{0.01}O_3$ thin film, which is much larger than that in previous reports in Nd-doped BFO under the same light intensity.

2. Materials and Methods

The BNFMO films were grown on 0.5-mm-thick single-crystal Nb (0.7 wt%)-doped $SrTiO_3$ (001) (NSTO) substrates via pulsed laser deposition (PLD). The substrates were first etched with a buffered hydrogen fluoride (BHF) solution before preparing the films, and then annealed in a furnace with flowing air at 950 °C for 2 h. A KrF excimer laser (λ = 248 nm) operating at 2 Hz was applied for target ablation, the laser fluence was 1.5 J/cm^2 with a spot area of 7.5 mm^2 on the target, and the target–substrate distance was set at 6.5 cm. The deposition was performed under an oxygen partial pressure of 0.1 Torr at a substrate temperature of 630 °C for 30 min.

The X-ray diffraction (XRD, λ = 1.5406 Å, Bruker, D8-ADVANCE, Karlsruhe, Germany) patterns of the BFO films were measured at room temperature. All XRD data were collected at 2θ ranges from 10° to 60° with a Cu X-ray source. The scan rate and step size of the collecting diffraction data were set as 0.02°/s and 0.02°/step, respectively. The morphologies

of NSTO substrates after annealing and BNFMO films were observed by scanning probe microscope (Multimode 8, Oxford Instruments, Oxford, UK). The ferroelectric domain switching and local piezoelectric responses were analyzed by the piezoresponse force microscopy (PFM) mode using a commercial atomic force microscope (AFM) (Asylum Research, MFP-3D, Oxford Instruments, Oxford, UK). The Au/BNFMO/NSTO/In heterojunction was prepared to study the characteristics of the leakage current density versus the applied electric field (*J–E*) and the dielectric properties of the BNFMO thin films. The top Au contacts with the thickness of 100 nm were deposited via sputtering as the top electrode, and square size of 200×200 μm was patterned in the liftoff process. Thicknesses of the films were obtained by the scanning electron microscope (SEM) (JSM-7001F, JEOL, Tokyo, Japan), and the amplification factor and acceleration voltage were set as 200,000 and 10 kV, respectively. Leakage currents were measured by a current source meter (2400, Keithley, Cleveland, OR, USA). All current data were collected from −2.5 to 2.5 V, and the voltage variation rate was set as 0.2 V. The electrical parameters of the materials were measured as a function of frequency (1 kHz^{-1} MHz) using a semiconductor electrical performance comprehensive tester (4200A-SCS, Cleveland, OR, USA). Additionally, the oscillating voltage amplitude was set as 0.5 V. The measurements of polarization current (*I–V*) and *P–V* loops were performed via a semiconductor device analyzer (WGFMU, B1500A, Agilent Technologies, Santa Clara, CA, USA) with the frequency of 10 KHz. The current density–voltage (*J–V*) curves were measured by a current source meter (2400, Keithley, Cleveland, OR, USA) when the films were illuminated with a 405 nm monochromatic laser. The light intensity was calibrated to 160 mW/cm^2 by an irradiation meter (FZ-A, photoelectric instrument factory of Beijing Normal University, Beijing, China).

3. Results and Discussion

Figure 1a demonstrates the surface topography of the etched substrate. Flat atomic-level steps separated were observed in the inset of Figure 1a. Figure 1b shows the cross-sectional SEM image of the BNFMO (40 nm) thin film grown on a NSTO substrate. The X-ray diffraction and Raman spectra were recorded to determine the crystal structure of the BNFMO (x = 0.00~0.20) thin films. Figure 1c shows XRD patterns of the BNFMO film on the Nb-doped SrTiO$_3$ (001) substrates grown at 630 °C. All films present the perovskite structure with the (001) orientation. In all the BNFMO films, there is no impurity and second phase observed, which indicates that Nd^{3+} and Mn^{4+} ions have entirely entered into the BFO lattice. The diffraction peaks of the thin films shift to the higher angle region with the increase in neodymium content. It is because Nd^{3+} ions with smaller ionic radius (0.995 Å) are substitutes for Bi^{3+} ions with a relatively smaller ionic radius (1.03 Å) on A sites, which leads to the lattice contraction. Additionally, there may be a tetragonal or orthorhombic structure transition induced by the Nd-doping elements according to the previous reports [16,38], which can be further confirmed by Raman spectra.

Figure 1d shows the Raman spectra of the BNFMO (x = 0.00~0.20) films at room temperature. Three A$_1$ vibration modes and seven E vibration modes are observed in the rhombohedral BiFeO$_3$ (the E vibration mode with low wavenumbers below 100 cm^{-1} was not detected), and the crystal structure is determined by comparing the relative positions of the characteristic vibration modes [39]. The modes of A$_1$-1, A$_1$-2, and A$_1$-3 are related to the vibration of the Bi-O bond, while the modes of A$_1$-4 and E are closely related to the vibration of the Fe-O bond. In the range of x = 0.00~0.16, the peak strength of the A$_1$-1 and A$_1$-2 modes enhances drastically and reaches the maximum at x = 0.16, thereby indicating that the electron cloud of the Bi-O bond and the bond angle of the Fe-O bond have changed [16]. The Raman peaks at 139, 172, 227, 262, 279, 373, 474, and 529 cm^{-1} of the thin BNFO (x = 0.00~0.16) films are assigned to the vibration modes of A$_1$-1, A$_1$-2, A$_1$-3, E-3, E-4, E-5, A$_1$-4, and E-9, as shown in Figure 1d. The result indicates that the BNFMO (x = 0.00~0.16) films are still rhombohedral bismuth ferrite. The positions of the characteristic peaks are exceedingly close to that of the trigonal phase block and thin BiFeO$_3$ film reported in the literature. Therefore, the original rhombohedral structure is

not changed when the Nd ion doping is below 16%. In addition, the E-8 mode gradually strengthens and widens with the increase in Nd-doping amount. This change is consistent with the tendency of transition from R3c to Pbnm phase structure [40]. When the doping amount reached 20%, the intensity of A_1-1, A_1-2, and A_1-3 modes decreases greatly, the vibration modes of E-3, E-4, and E-8 are shifted, respectively, to 268, 288, 548 cm^{-1}, and the E-5 vibration mode disappeared. This behavior indicates a strong variation in Bi-O and Fe-O-Fe bonds and a transformation from rhombohedral to orthorhombic structure for the $Bi_{0.80}Nd_{0.20}Fe_{0.99}Mn_{0.01}O_3$ film [41].
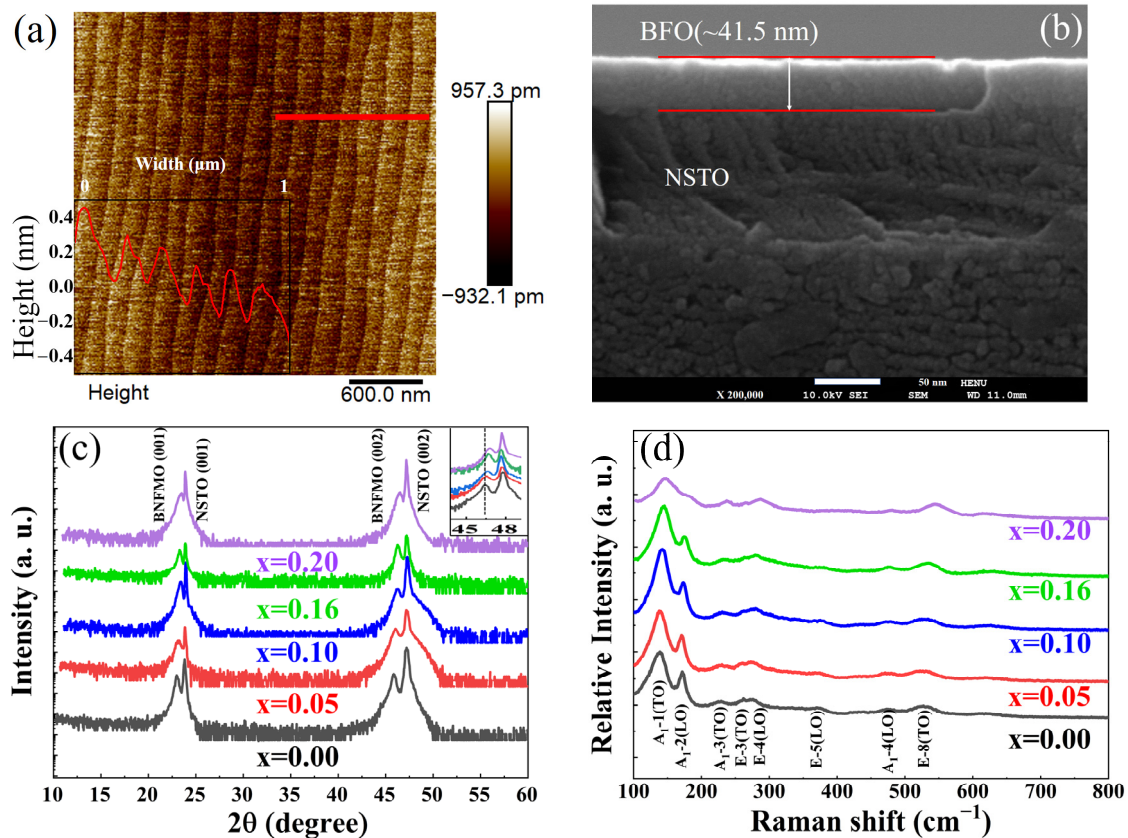

Figure 1. (**a**) Etched topography of NSTO substrate. (**b**) Microscopic SEM cross-sectional image of a $Bi_{0.84}Nd_{0.16}Fe_{0.99}Mn_{0.01}O_3$ thin film on a NSTO substrate. (**c**) 2θ-XRD patterns of $Bi_{1-x}Nd_xFe_{0.99}Mn_{0.01}O_3$/NSTO heterojunctions (x = 0.00~0.20). (**d**) Raman spectra for BNFMO films at room temperature.

Figure 2a shows the surface morphologies of the $Bi_{1-x}Nd_xFe_{0.99}Mn_{0.01}O_3$/NSTO heterojunctions (x = 0.00~0.20). There are low density holes on the surface of the $BiFe_{0.99}Mn_{0.01}O_3$ film with square root roughness of 1.93 ($\pm$0.19) nm. Moreover, all BNFMO (x = 0.05, 0.10, 0.16, 0.20) films exhibit a uniform and crack-free microstructure with a thickness of 40 nm, and the square root roughness is 1.62 ($\pm$0.12) nm, 1.21 ($\pm$0.08) nm, 0.98 ($\pm$0.05) nm, and 1.49 ($\pm$0.11) nm, respectively. Figure 3a–e demonstrates the grain size histogram and Gaussian fitting of BNFMO (x = 0.00~0.20) films. As shown in Figure 3, the grain size reduces slightly with the increase in Nd concentration, which is caused by more and more Nd ions stacked at the grain boundaries and preventing the grain from growing up with the increase in Nd concentration. Additionally, it may also be due to the substitution of Bi^{3+} by Nd^{3+}, protecting the Bi^{3+} from volatilizing during the sintering process; thus, reducing the generation of oxygen vacancy content. The reduction will relatively reduce the oxygen content of films during the preparation of the films, which will also decrease the growth speed of grains [42,43]. The average grain sizes of BNFMO (x = 0.00, 0.05, 0.10, 0.16, 0.20) films are 98 ($\pm$5), 87 ($\pm$5), 73 ($\pm$3), 68 ($\pm$3), and 47 ($\pm$4) nm, respectively.
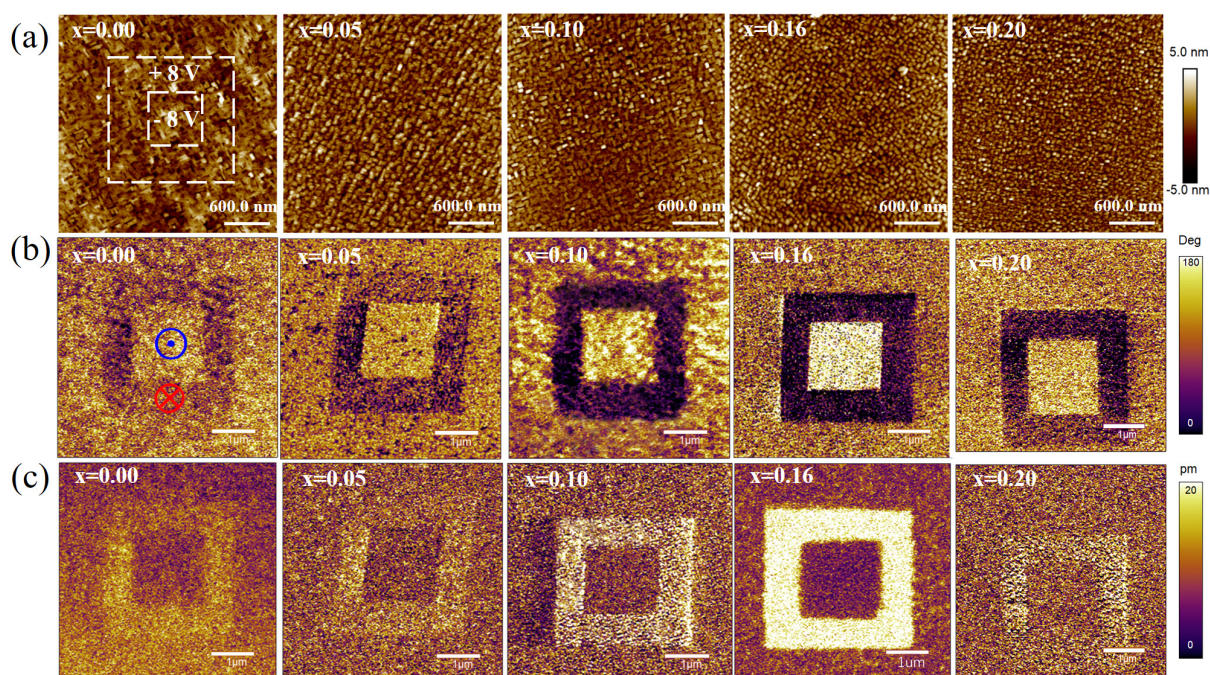
Figure 2. (**a**) The 2D AFM images of BNFMO (x = 0.00~0.20) thin films. (**b**) PFM phase and (**c**) amplitude plots of BNFMO (x = 0.00~0.20) thin films.
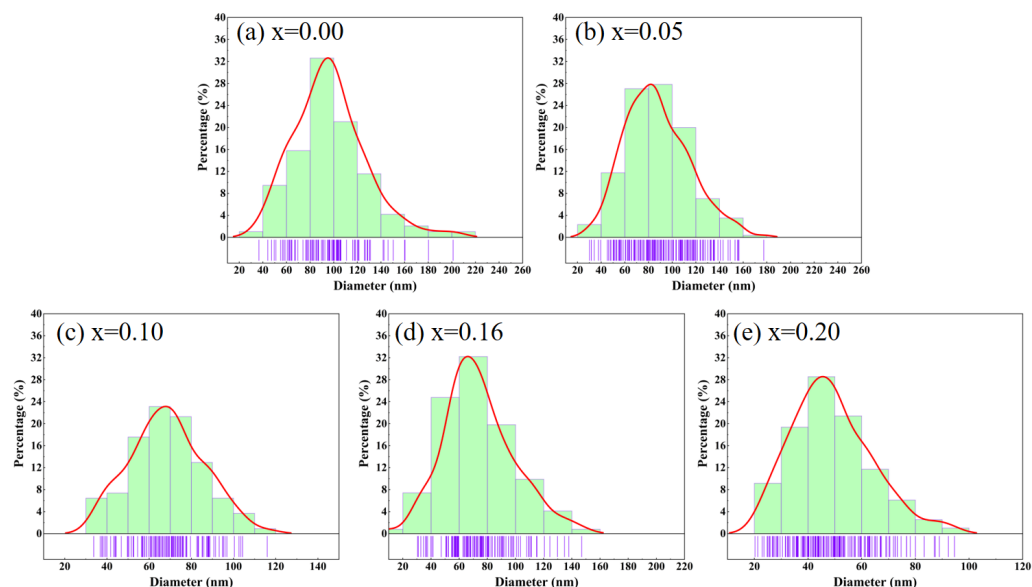

Figure 3. Histograms for particle size distribution and Gaussian fitting curve of (**a–e**) BNFMO (x = 0.00, 0.05, 0.10, 0.16, 0.20) films.

As shown in Figure 2b,c, we adopted piezoresponse force microscopy (PFM) to obtain the local ferroelectric properties of the BNFMO films. The acquired PFM out-of-plane phase and amplitude images were acquired after applying −8 and +8 V biases on the surface of the BNFMO films. Based on the PFM results, the polarization reversal becomes more apparent when the doping amount of Nd ion increases from 0 to 16%, which is ascribed to the enhanced ion or electron displacement polarization caused by Nd ions [16]. When the doping amount of Nd ion reached 20%, the contrast of the phase and amplitude out of the plane became lower which is due to the formation of the orthorhombic structure of the film. The results are consistent with the Raman spectrum.

Figure 4 shows the characteristics of the leakage current versus the applied voltage (I–V) and dielectric properties of the BNFMO films. The leakage current of the BNFMO (x = 0.00~0.16) films decreased significantly with the increase in the Nd ion concentration, as shown in Figure 4a. The inset of Figure 4a shows the structure of the device used for the measurement. The reduction in oxygen vacancy content and other impurity defects leads to poor local conductivity, which is consistent with other reports reducing oxygen vacancy concentration by replacing a volatile Bi ion with a nonvolatile Nd ion. However, due to the excessive doping, there are more defect charges with the $Bi_{0.80}Nd_{0.20}Fe_{0.99}Mn_{0.01}O_3$ thin film; thus generating an increase in leakage current compared to $Bi_{0.84}Nd_{0.16}Fe_{0.99}Mn_{0.01}O_3$ film [44]. Figure 4b illustrates a systematic reduction in dielectric permittivity ($\mathcal{E}_r$) of BNFMO (x = 0.00~0.20) films with Nd-doping [42] at high frequencies, which is attributed to the polarization relaxation phenomenon. It can be ascribed to fact that the contribution of interfacial, dipolar, ionic, and atomic polarizations decreases with increasing frequency and finally vanishes (except electronic polarization) at extremely high frequencies [45,46]. The $\mathcal{E}_r$ of the $Bi_{0.80}Nd_{0.20}Fe_{0.99}Mn_{0.01}O_3$ thin film reduced drastically at a low frequency, but this phenomenon is absent on the BNFMO (x = 0.00, 0.05, 0.10, 0.16) thin film, thereby indicating more defect charges in the $Bi_{0.8}Nd_{0.20}Fe_{0.99}Mn_{0.01}O_3$ film, such as Fe^{2+}. Meanwhile, the increase in the doping amount of Nd ion tends to decrease the dielectric permittivity of the BNFMO (x = 0.00~0.20) thin films at low frequency, and the dielectric permittivity is 612, 589, 499, 471, and 435 at 1 kHz, respectively, which is increased from the decrease in grain size and the reduction in space charge polarization and conductivity of the sample [47,48]. Significantly, the $Bi_{0.8}Nd_{0.20}Fe_{0.99}Mn_{0.01}O_3$ film shows the highest dielectric loss (tan δ) at low frequency as shown in Figure 4c. The increase in the tan δ and decrease in the $\mathcal{E}_r$ of $Bi_{0.8}Nd_{0.20}Fe_{0.99}Mn_{0.01}O_3$ film indicates the strong dielectric relaxation behavior in film [16].

Positive-up–negative-down (PUND) was generally adopted to measure the ferroelectric properties, in which five triangular pulse signals were implemented, and the PUND measurement effectively removed the effects of the leakage current, dielectric current, and experimental setup (R, L). The measured currents included polarization current (I_F), leakage current (I_L), and dielectric current (I_ε). The ferroelectric (FE) polarization currents (I_{PUND}) in the negative and positive directions were defined as $I_{PUND-} = I_P - I_U = I_{F-}$ and $I_{PUND+} = I_N - I_D = I_{F+}$, respectively [49]. In this paper, the ferroelectric hysteresis loop of the BNFMO (x = 0.00~0.20) films was measured using the PUND method to eliminate the influence of leakage current. However, the resistive switching (RS) effect caused by the movement of oxygen vacancy content also causes erroneous polarization current values [50,51]. As shown in Figure 5a, the I_D current increases in the positive direction due to the occurrence of resistance switching (RS) current (I_S) from a high resistance state (HRS) to a low resistance state (LRS) in the fifth pulse (I_D). The current measured in the positive direction ($I_{PUND+} = I_N - I_D = I_{F+} - I_{S+}$) is lower than the actual ferroelectric polarization current (I_{F+}). On the contrary, I_{PUND-} current exceeds the actual I_{F-} ($I_{PUND-} = I_P - I_U = I_{F-} + I_{S-}$). Therefore, the measured current I_{PUND-} exceeds the actual ferroelectric polarization switching current (I_{F-}) [49]. Thus, the existence of the resistive switching effect still leads to the incorrect P–V loop of BNFMO films whose polarization (−) (P_{r-}) value observably exceeded the polarization (+) (P_{r+}) value.

In this study, in order to deduct the influence of the RS effect during the PUND measurement, the PUND measurement was carried out for BNFMO (x = 0.00~0.20) connected in series with single and back-to-back connected two identical 40-nm-thick BNFMO ferroelectric capacitors, respectively. Firstly, we selected $Bi_{0.84}Nd_{0.16}Fe_{0.99}Mn_{0.01}O_3$ film to study the two different measurement approaches. Figure 5a shows the PUND measurement on $Bi_{0.84}Nd_{0.16}Fe_{0.99}Mn_{0.01}O_3$ film of a single device and two devices in series at 10 kHz. The inset shows the structure for two different measurement methods. The corresponding I–V and P–V loops of two different measurement methods were calculated from the blue and red lines of (a), respectively, as shown in Figure 5c–f. Obviously, as can be seen in Figure 4c,d, the abnormal I–V and P–V loops were observed, but Figure 5e,f

demonstrates the symmetrical loops. Furthermore, we measured the DC *I–V* curves of two different approaches to verify the PUND results. The voltage was applied in the order of 0 V → +5 V (2.5 V) → 0 V → −5 V (−2.5 V) → 0 V, as shown in Figure 5b. The observed results of PUND and DC *I–V* curves indicate that the structure of two devices in series can reduce the RS effect effectively. When we measure the ferroelectric hysteresis loop, the maximum range of the test instrument is −5 to +5 V. Thereby, if the two devices in series technique is used, the measurement range is only −2.5−2.5 V, which will lead to the *P–V* loop we measured being unable to reach saturation polarization [52,53]. Hence, further measurements were undertaken to verify the ferroelectric properties of the $Bi_{0.84}Nd_{0.16}Fe_{0.99}Mn_{0.01}O_3$ film. For ferroelectric material, the piezoresponse (*PR*) hysteresis loop is expected to deform and even collapse when V_{ac} is above the coercive voltage because the polarization switching counteracts the *PR* [54,55]. The phase, amplitude, and *PR* of the $Bi_{0.84}Nd_{0.16}Fe_{0.99}Mn_{0.01}O_3$ film were measured to verify the ferroelectric properties. This behavior is observed on the $Bi_{0.84}Nd_{0.16}Fe_{0.99}Mn_{0.01}O_3$ film in Figure 5g,h. This result indicates that $Bi_{0.84}Nd_{0.16}Fe_{0.99}Mn_{0.01}O_3$ thin films exhibit true ferroelectric properties.
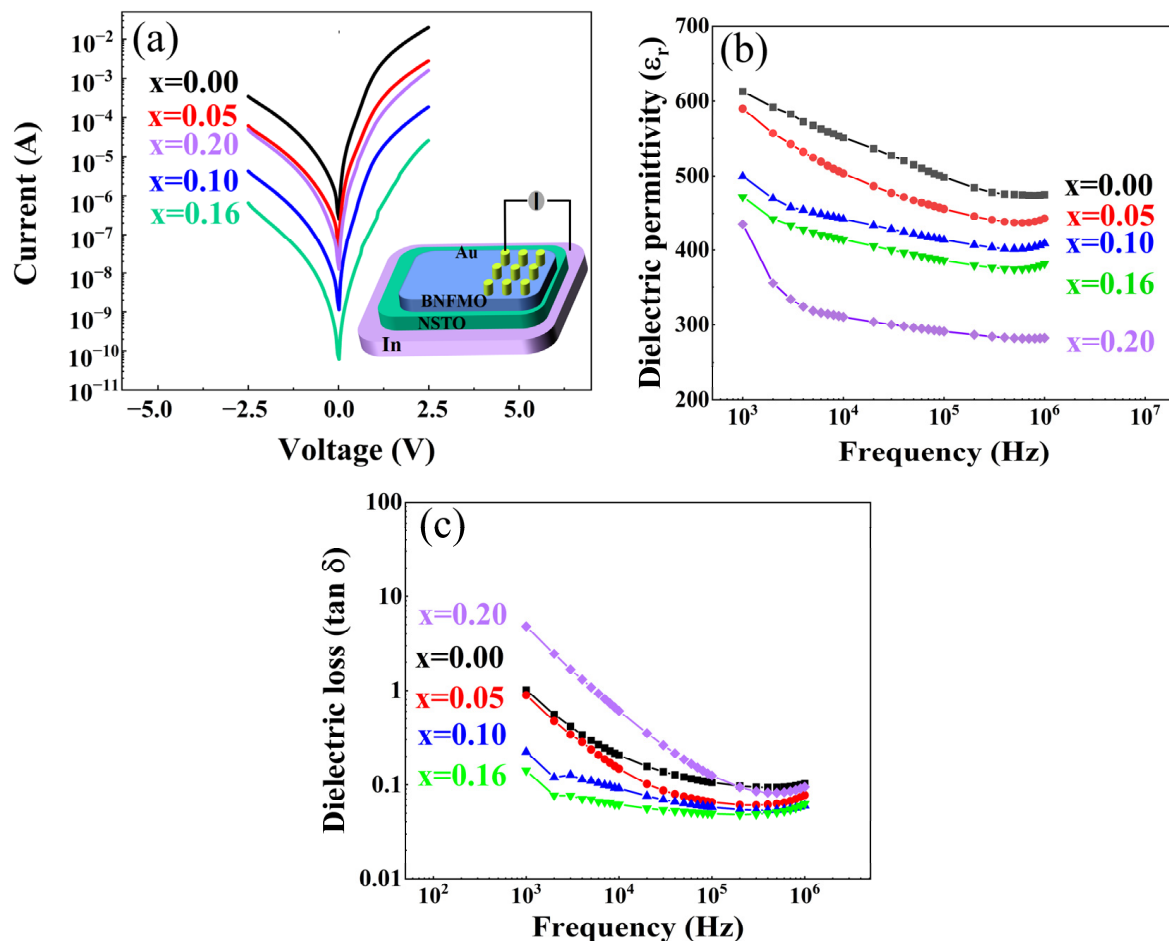

Figure 4. (**a**) Voltage dependence of leakage current of BNFMO films. The inset shows the schematic drawing of the device structure. (**b**) Dielectric permittivity ($\mathcal{E}_r$). (**c**) Dielectric loss (tan δ) of BNFMO films recorded at room temperature.

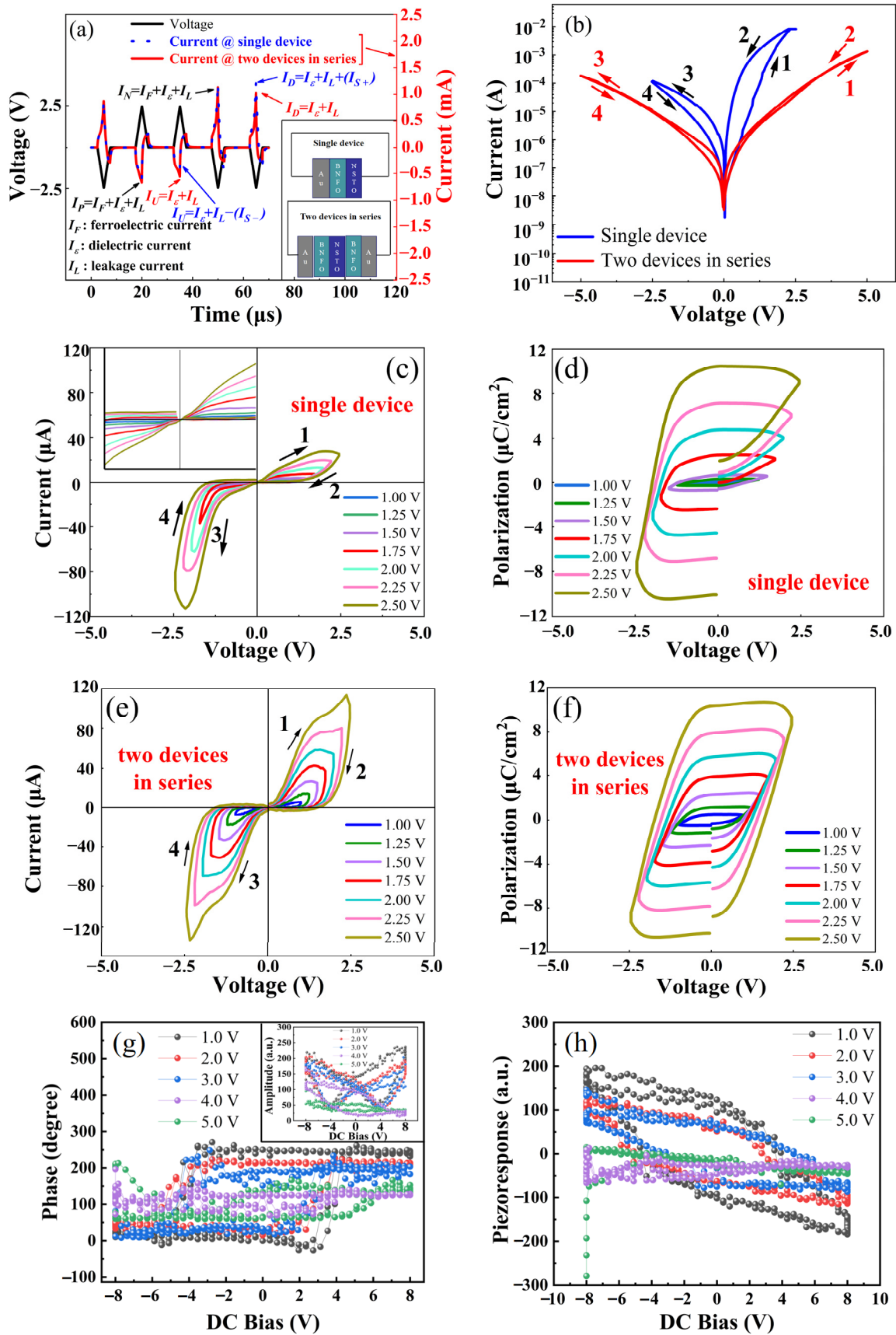**Figure 5.** (**a**) PUND measurement on $Bi_{0.84}Nd_{0.16}Fe_{0.99}Mn_{0.01}O_3$ film of two different structures at 10 kHz. The inset shows the structure for two different measurement methods. (**b**) DC *I–V* curves of $Au/Bi_{0.84}Nd_{0.16}Fe_{0.99}Mn_{0.01}O_3/NSTO/In$ are measured on two structures, respectively. (**c**) The *I–V*

loop and (**d**) *P–V* loop of single devices are calculated from the blue line of (**a**). (**e**) The *P–V* loop and (**f**) *I–V* loop of two devices in series are calculated from the red line of (**a**). (**g**) PFM amplitude and phase loops were measured with V_{ac} (1 V~5 V) on bare $Bi_{0.84}Nd_{0.16}Fe_{0.99}Mn_{0.01}O_3$ surface. (**h**) Piezoresponse (*PR*) of $Bi_{0.84}Nd_{0.16}Fe_{0.99}Mn_{0.01}O_3$ film with the formula of $PR = A \cos \theta$.

The approach of two devices in series was further extended to all BNFMO (x = 0.00~0.20) thin films. Two 40-nm-thick BNFO films with the same doping amount were connected in series. Figure 6a presents the *P–V* and *I–V* loops of five BNFO films measured by the PUND measurement, in which two devices were in series at 2.5 V with a driving frequency of 10 kHz. Figure 6b shows the schematic diagram of the remnant polarization (P_r) and coercive voltages of BNFMO films vary with increasing Nd-doping concentration. It can be seen that the P_r enhances and coercive voltage reduces, respectively, with the increase in Nd ion concentration in the BNFMO (x = 0.00~0.16) films. Additionally, the hysteresis loops of the films, with P_r of approximately 2.9, 4.3, 5.5, and 10.7 $\mu C/cm^2$, respectively, were successfully obtained. The P_r and coercive voltage values reached the maximum and minimum at x = 0.16, which can be attributed to the enhanced ion or electron displacement polarization caused by Nd ion and the reduction in the leakage current [56]. However, when the doping amount of Nd ions reaches 20%, the P_r of the film greatly decreases from 10.7 to 4.9 $\mu C/cm^2$ and the coercive voltage increases from 1.70 to 1.75 V, which are attributed to transformation from rhombohedral to the orthogonal structure and paraelectricity of the film. During the variation of x = 0.16–0.20, the crystal structure parameters only change slowly, so the stereochemical activity should have the predominant effect on the observed ferroelectric–paraelectric transition [56,57].
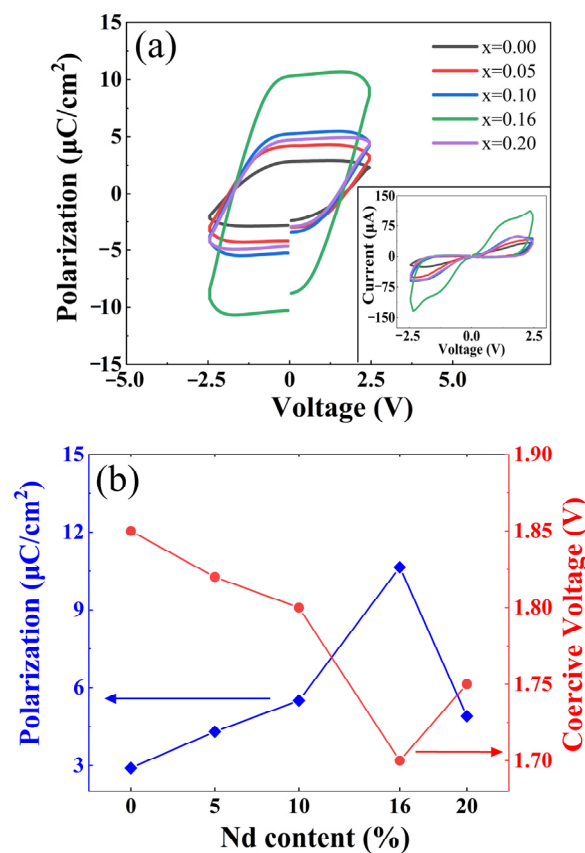

Figure 6. (**a**) The *P–V* and *I–V* loops of BNFMO films are calculated from two devices in series. (**b**) The change in the remnant polarization and coercive voltage values with Nd-doping amount.

The photovoltaic characteristics of Au/BNFMO/NSTO/In ferroelectric photovoltaic devices were measured with a 405 nm monochromatic laser as the excitation light source. Figure 7a,b presents *I–V* photovoltaic characteristic diagrams of the ferroelectric photovoltaic device under light and dark environments, and the circuit connection diagram of the ferroelectric photovoltaic devices is shown in the inset of Figure 7b. Compared with the dark environment, the open-circuit voltage (V_{oc}) and short-circuit (I_{sc}) current of films increase to a certain extent under illumination, implying that the photo-generated carriers under illumination results in the formation of photo-generated voltage and current, which verifies the photovoltaic effect of films. Generally speaking, there is no signal output in the dark environment, and the experimental results show that there is open circuit voltage and short circuit current, which is because there is an interface in the ferroelectric photovoltaic device, and there would be many defects on the interface, in which the defect charge and vacancy charge will form an internal electric field [34]. As a result, it causes the BNFMO films to also exhibit V_{oc} and I_{sc} in a dark environment.
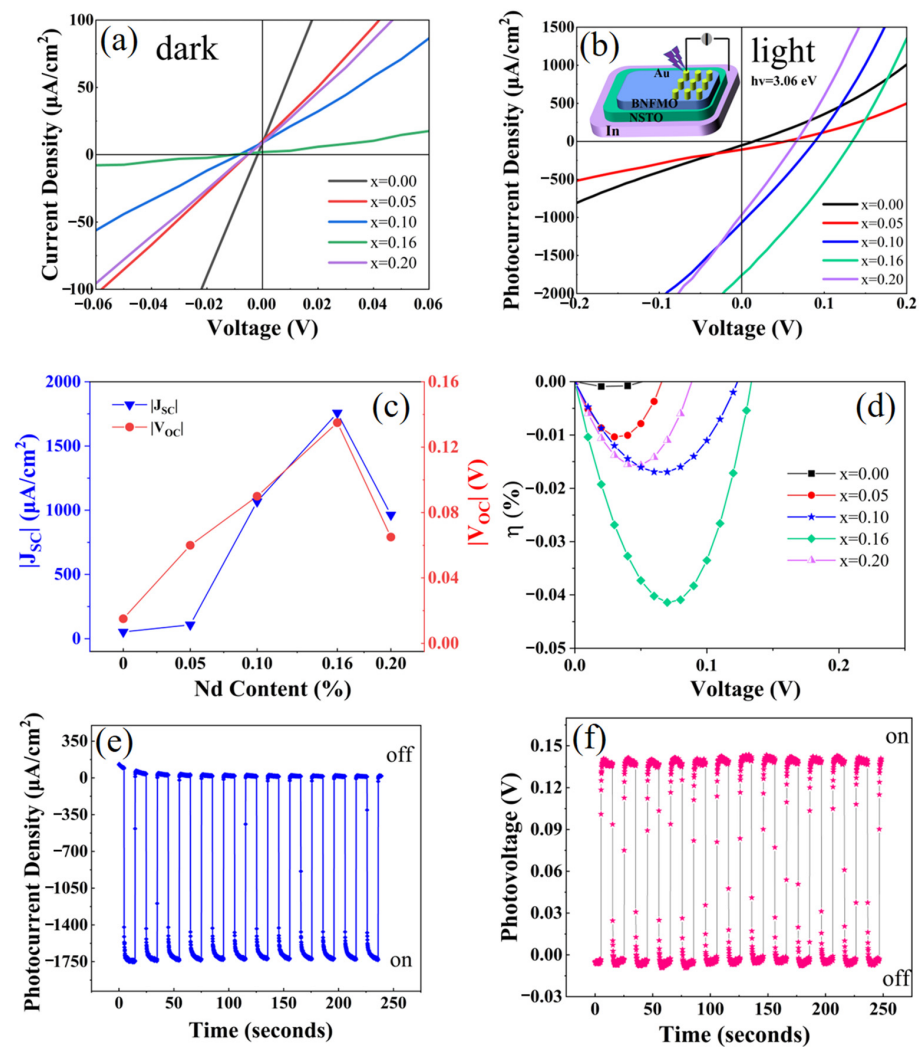

Figure 7. (**a**) *J–V* curves of ferroelectric photovoltaic devices in darkness. (**b**) *J–V* curves of ferroelectric photovoltaic devices under illumination. The inset shows the Au/BNFMO (x = 0.00~0.20)/NSTO/In structure diagram of the ferroelectric photovoltaic device. (**c**) The change in the J_{SC} and V_{OC} with Nd-doping amount. (**d**) Corresponding voltage dependence of light-to-electricity power conversion efficiency (η) for $BiFe_{0.99}Mn_{0.01}O_3$ film with different Nd^{3+} contents. (**e**,**f**) The time dependence of the photocurrent density and photovoltage of $Bi_{0.84}Nd_{0.16}Fe_{0.99}Mn_{0.01}O_3$.

The Nd-doping not only reduces the dark current density but also raises the photocurrent density, and the $Bi_{0.84}Nd_{0.16}Fe_{0.99}Mn_{0.01}O_3$ thin film exhibits a more than 35-fold enhancement compared with the BFMO film, indicating that the ferroelectric photovoltaic effect is regulated by the ferroelectric polarization. The photocurrent densities of BNFMO (x = 0.00~0.20) films are -52, -108, -1067, -1758, and -964 $\mu A/cm^2$, while the photovoltages are 0.020, 0.050, 0.090, 0.135, and 0.065 V, respectively. Figure 7c demonstrates the change in the J_{SC} and V_{OC} with Nd-doping amount. The power conversion efficiencies ($\eta = P_{out}/P_{in} = JV/P_{in}$) at the point (J, V) of the BNFMO films are shown in Figure 7d. To verify the reliability of the ferroelectric photovoltaic phenomenon, we measured the time dependence of the photocurrent density and photovoltage of $Bi_{0.84}Nd_{0.16}Fe_{0.99}Mn_{0.01}O_3$ film by controlling the light source to turn on and off alternately every 12.5 s, as shown in Figure 7e,f. Obviously, there is no attenuation of the photocurrent density and photovoltage during several cycles. In addition, it should be noted that our experimental results are numerically much larger in short-circuit current compared to reported literature results of Nd-doped BFO. Table 1 presents a comparison of photocurrent density performance for ion-doped BFO films. Compared with the other reported ion-doped BFO films, the J_{SC} of the $Bi_{0.84}Nd_{0.16}Fe_{0.99}Mn_{0.01}O_3$ film in this work is quite competitive. The enhanced photocurrent property depends on five aspects. Firstly, the $Bi_{0.84}Nd_{0.16}Fe_{0.99}Mn_{0.01}O_3$ film prepared by us with an appropriate thickness. Qin et al. [29] found that the ferroelectric film with a thickness of approximately 30–40 nm demonstrated the strongest photocurrent. Secondly, the crystal structure of the epitaxial thin film has minimal defects, enhancing the lifetime of photogenerated carriers. Thirdly, we utilized a relatively high dielectric constant NSTO as the bottom electrode. The high-dielectric-constant electrode tends to distribute the screening charges more widely away from the interface; thus, weakening the polarization screening effect. Fourthly, the electrons and holes can be separated effectively by the large depolarization field which derived from a larger remnant polarization. Finally, Shi et al. [32] reported that the band gap of the BFO film was reduced by Nd-doping, which allows to collect solar spectrum energy effectively for BFO film. Thus, a larger short circuit photocurrent density (1758 $\mu A/cm^2$) was generated by $Bi_{0.84}Nd_{0.16}Fe_{0.99}Mn_{0.01}O_3$ film.

Table 1. Comparison of photovoltaic performance and thickness for doped BFO films.

Samples	Light Intensity (mW cm^{-2})	J_{SC} (mA cm^{-2})	V_{OC} (V)	Film Thickness (nm)	References
$Bi_{0.84}Nd_{0.16}Fe_{0.99}Mn_{0.01}O_3$	160	1.758	0.135	40	This work
$Bi_{0.9}Nd_{0.1}FeO_3$	100	0.048	0.7	700	[32]
$Bi_{0.95}Nd_{0.05}FeO_3$	100	0.035	0.2	150–190	[34]
$BiFe_{0.92}Ti_{0.08}O_3$	100	0.020	0.52	-	[58]
$Bi_{0.8}Na_{0.2}FeO_3$	100	0.001	0.625	-	[59]
$Bi_{0.9}Sr_{0.1}FeO_{3-\delta}$	100	0.036	0.42	300	[60]
$BiFe_{0.6}Sc_{0.4}O_3$	22.3	0.0065	0.6	200	[61]
$Bi_{0.88}Ce_{0.12}Fe_{0.9}Mn_{0.1}O_3$	160	0.036	0.25	350	[62]
$Bi_{0.95}Nd_{0.05}Fe_{0.97}V_{0.03}O_3$	100	0.0985	0.65	-	[20]
$Bi_{0.975}La_{0.025}Fe_{0.975}Ni_{0.025}O_3$	5	0.00135	0.67	600	[63]
$BiNd_{0.03}FeO_3$	1000–3000	12.1	0.81	170	[64]
$BiFe_{0.95}Mn_{0.05}O_3$	2500	0.015	3.1	300	[26]
Bi_2FeCrO_6	100	20.6	0.84	100	[27]
$BiFe_{0.95}Si_{0.05}O3$	100	23.8	0.45	650	[28]

4. Conclusions

In summary, $Bi_{1-x}Nd_xFe_{0.99}Mn_{0.01}O_3$ (x = 0.00~0.20) films with a thickness of 40 nm were prepared on Nb-doped $SrTiO_3$ substrates by PLD to form Au/BNFMO/NSTO heterojunctions. The original rhombohedral structure of the $BiFeO_3$ thin films remained when the doping amount of Nd ion was less than 16%, while the BNFO thin film structure became orthogonal when the doping amount of Nd^{3+} ion reached 20%. To avoid the resistive switching effect and decrease the leakage current, the structure of two de-

vices in series was adopted for ferroelectric hysteresis loop measurement. The maximum remnant polarization (P_r) and minimum coercive voltage (V_c) were obtained under the condition of 16% Nd-doping. In addition, we obtained the maximum photocurrent density of 1758 $\mu A/cm^2$ in $Bi_{0.84}Nd_{0.16}Fe_{0.99}Mn_{0.01}O_3$ thin film. This is larger than that in previous reports in Nd-doped BFO films under the same light intensity.

Thus, the BNFMO films show great potential for ferroelectric and photovoltaic applications.

Author Contributions: Conceptualization, Q.W.; methodology, Q.W. and Z.G.; software, Q.W.; validation, Q.W., Y.S., Z.G. and C.J.; formal analysis, Q.W., Z.G. and C.J.; investigation, Q.W. and Y.S.; resources, Q.W., Z.G., C.J. and W.Z.; data curation, Q.W.; writing—original draft preparation, Q.W.; writing—review and editing, Q.W., Y.S., C.J. and W.Z.; funding acquisition, C.J. and W.Z. All authors have read and agreed to the published version of the manuscript.

Data Availability Statement: All data that support the findings of this study are included within the article.

Conflicts of Interest: The authors declare no competing financial interest.

References

1. Nakamura, Y.; Nakashima, S.; Ricinschi, D.; Okuyama, M. The Insertion Effect of Bi-excess Layers on Stoichiometric BiFeO₃ Thin Films Prepared by Chemical Solution Deposition. *Funct. Mater. Lett.* **2008**, *1*, 19–24. [CrossRef]
2. Neaton, J.B.; Ederer, C.; Waghmare, U.V.; Spaldin, N.A.; Rabe, K.M. First-principles study of spontaneous polarization in multiferroic BiFeO₃. *Phys. Rev. B* **2005**, *71*, 014113. [CrossRef]
3. Martin, L.W.; Chu, Y.H.; Ramesh, R. Advances in the growth and characterization of magnetic, ferroelectric, and multiferroic oxide thin films. *Mater. Sci. Eng. R Rep.* **2010**, *68*, 89–133. [CrossRef]
4. Korkmaz, S.; Kariper, I.A. Pyroelectric nanogenerators (PyNGs) in converting thermal energy into electrical energy: Fundamentals and current status. *Nano Energy* **2021**, *84*, 105888. [CrossRef]
5. Korkmaz, S.; Kariper, I.A. Production and applications of flexible/wearable triboelectric nanogenerator (TENGS). *Synth. Met.* **2021**, *273*, 116692. [CrossRef]
6. Korkmaz, S.; Kariper, I.A. Aerogel based nanogenerators: Production methods, characterizations and applications. *Int. J. Energy Res.* **2020**, *44*, 11088–11110. [CrossRef]
7. Korkmaz, S.; Kariper, I.A. BaTiO₃-based nanogenerators: Fundamentals and current status. *J. Electroceram.* **2021**. [CrossRef]
8. Singh, S.K.; Ishiwara, H.; Maruyama, K. Enhanced polarization and reduced leakage current in BiFeO₃ thin films fabricated by chemical solution deposition. *J. Appl. Phys.* **2006**, *100*, 064102. [CrossRef]
9. Kim, J.W.; Raghavan, C.M.; Kim, Y.-J.; Oak, J.-J.; Kim, H.J.; Kim, W.-J.; Kim, M.H.; Song, T.K.; Kim, S.S. Electrical properties of chemical solution deposited (Bi₀.₉RE₀.₁)(Fe₀.₉₇₅Cu₀.₀₂₅)O₃-delta (RE = Ho and Tb) thin films. *Ceram. Int.* **2013**, *39*, S189–S193. [CrossRef]
10. Sharma, H.B.; Singh, N.B.; Devi, K.N.; Lee, J.H.; Singh, S.B. Structural and optical properties of manganese substituted nanocrystalline bismuth ferrite thin films by sol-gel process. *J. Alloys Compd.* **2014**, *583*, 106–110. [CrossRef]
11. Tang, X.; Dai, J.; Zhu, X.; Sun, Y. In situ magnetic annealing effects on multiferroic Mn-doped BiFeO₃ thin films. *J. Alloys Compd.* **2013**, *552*, 186–189. [CrossRef]
12. Jin, L.; Li, F.; Zhang, S. Decoding the Fingerprint of Ferroelectric Loops: Comprehension of the Material Properties and Structures. *J. Am. Ceram. Soc.* **2014**, *97*, 1–27. [CrossRef]
13. Shi, X.X.; Liu, X.Q.; Chen, X.M. Structure evolution and piezoelectric properties across the morphotropic phase boundary of Sm-substituted BiFeO₃ ceramics. *J. Appl. Phys.* **2016**, *119*, 064104. [CrossRef]
14. Noguchi, Y.; Matsuo, H.; Kitanaka, Y.; Miyayama, M. Ferroelectrics with a controlled oxygen-vacancy distribution by design. *Sci. Rep.* **2019**, *9*, 4225. [CrossRef]
15. Zhang, D.H.; Shi, P.; Wu, X.Q.; Ren, W. Structural and electrical properties of sol-gel-derived Al-doped bismuth ferrite thin films. *Ceram. Int.* **2013**, *39*, S461–S464. [CrossRef]
16. Xue, X.; Tan, G.; Liu, W.; Hao, H. Study on pure and Nd-doped BiFeO₃ thin films prepared by chemical solution deposition method. *J. Alloys Compd.* **2014**, *604*, 57–65. [CrossRef]
17. Xue, X.; Tan, G.Q. Effect of bivalent Co ion doping on electric properties of Bi₀.₈₅Nd₀.₁₅FeO₃ thin film. *J. Alloys Compd.* **2013**, *575*, 90–95. [CrossRef]

18. Maleki, H.; Zare, S.; Fathi, R. Effect of Nd Substitution on Properties of Multiferroic Bismuth Ferrite Synthesized by Sol-Gel Auto-combustion Method. *J. Supercond. Nov. Magn.* **2018**, *31*, 2539–2545. [CrossRef]

19. Kawae, T.; Tsuda, H.; Morimoto, A. Reduced leakage current and ferroelectric properties in Nd and Mn codoped $BiFeO_3$ thin films. *Appl. Phys. Express* **2008**, *1*, 051601. [CrossRef]

20. Agarwal, R.; Sharma, Y.; Hong, S.; Katiyar, R.S. Modulation of oxygen vacancies assisted ferroelectric and photovoltaic properties of (Nd, V) co-doped $BiFeO_3$ thin films. *J. Phys. D Appl. Phys.* **2018**, *51*, 275303. [CrossRef]

21. Kawae, T.; Tsuda, H.; Naganuma, H.; Yamada, S.; Kumeda, M.; Okamura, S.; Morimoto, A. Composition dependence in $BiFeO_3$ film capacitor with suppressed leakage current by Nd and Mn cosubstitution and their ferroelectric properties. *Jpn. J. Appl. Phys.* **2008**, *47*, 7586–7589. [CrossRef]

22. Bhatnagar, A.; Chaudhuri, A.R.; Kim, Y.H.; Hesse, D.; Alexe, M. Role of domain walls in the abnormal photovoltaic effect in $BiFeO_3$. *Nat. Commun.* **2013**, *4*, 2835. [CrossRef]

23. Wu, J.G.; Fan, Z.; Xiao, D.Q.; Zhu, J.G.; Wang, J. Multiferroic bismuth ferrite-based materials for multifunctional applications: Ceramic bulks, thin films and nanostructures. *Prog. Mater. Sci.* **2016**, *84*, 335–402. [CrossRef]

24. Seidel, J.; Fu, D.Y.; Yang, S.Y.; Alarcon-Llado, E.; Wu, J.Q.; Ramesh, R.; Ager, J.W. Efficient Photovoltaic Current Generation at Ferroelectric Domain Walls. *Phys. Rev. Lett.* **2011**, *107*, 126805. [CrossRef] [PubMed]

25. Nakashima, S.; Higuchi, T.; Yasui, A.; Kinoshita, T.; Shimizu, M.; Fujisawa, H. Enhancement of photovoltage by electronic structure evolution in multiferroic Mn-doped $BiFeO_3$ thin films. *Sci. Rep.* **2020**, *10*, 15108. [CrossRef] [PubMed]

26. Matsuo, H.; Noguchi, Y.; Miyayama, M. Gap-state engineering of visible-light-active ferroelectrics for photovoltaic applications. *Nat. Commun.* **2017**, *8*, 207. [CrossRef]

27. Nechache, R.; Harnagea, C.; Li, S.; Cardenas, L.; Huang, W.; Chakrabartty, J.; Rosei, F. Bandgap tuning of multiferroic oxide solar cells. *Nat. Photonics* **2015**, *9*, 61–67. [CrossRef]

28. Gupta, S.; Medwal, R.; Limbu, T.B.; Katiyar, R.K.; Pavunny, S.P.; Tomar, M.; Morell, G.; Gupta, V.; Katiyar, R.S. Graphene/semiconductor silicon modified $BiFeO_3$/indium tin oxide ferroelectric photovoltaic device for transparent self-powered windows. *Appl. Phys. Lett.* **2015**, *107*, 062902. [CrossRef]

29. Meng, Q.; Yao, K.; Liang, Y.C. Photovoltaic mechanisms in ferroelectric thin films with the effects of the electrodes and interfaces. *Appl. Phys. Lett.* **2009**, *95*, 233. [CrossRef]

30. Qin, M.; Yao, K.; Liang, Y.C. Photovoltaic characteristics in polycrystalline and epitaxial $(Pb_{0.97}La_{0.03})(Zr_{0.52}Ti_{0.48})O_3$ ferroelectric thin films sandwiched between different top and bottom electrodes. *J. Appl. Phys.* **2009**, *105*, 061624. [CrossRef]

31. Qin, M.; Yao, K.; Liang, Y.C. High efficient photovoltaics in nanoscaled ferroelectric thin films. *Appl. Phys. Lett.* **2008**, *93*, 122904. [CrossRef]

32. Shi, T.J.; Wang, J.H.; Yan, W.; Shao, X.H.; Hou, Z.L. Enhanced photovoltaic property based on reduced leakage current and band gap in Nd-doped $BiFeO_3$ films. *Mater. Res. Express* **2019**, *6*, 086426. [CrossRef]

33. Zhang, J.Y.; Ma, P.P.; Shi, T.J.; Shao, X.H. Nd-Cr co-doped $BiFeO_3$ thin films for photovoltaic devices with enhanced photovoltaic performance. *Thin Solid Film.* **2020**, *698*, 137852. [CrossRef]

34. Tan, K.H.; Chen, Y.W.; Van, C.N.; Wang, H.L.; Chen, J.W.; Lim, F.S.; Chew, K.H.; Zhan, Q.; Wu, C.L.; Chai, S.P.; et al. Energy Band Gap Modulation in Nd-Doped $BiFeO_3$/$SrRuO_3$ Heteroepitaxy for Visible Light Photoelectrochemical Activity. *Acs Appl. Mater. Interfaces* **2019**, *11*, 1655–1664. [CrossRef]

35. Biswas, P.P.; Pal, S.; Subramanian, V.; Murugavel, P. Large photovoltaic response in rare-earth doped $BiFeO_3$ polycrystalline thin films near morphotropic phase boundary composition. *Appl. Phys. Lett.* **2019**, *114*, 173901. [CrossRef]

36. Wu, J.G.; Wang, J.; Xiao, D.Q.; Zhu, J.G. Mn^{4+}:$BiFeO_3$/Zn^{2+}:$BiFeO_3$ bilayered thin films of (111) orientation. *Appl. Surf. Sci.* **2011**, *257*, 7226–7230. [CrossRef]

37. Qi, X.D.; Wei, M.; Lin, Y.; Jia, Q.X.; Zhi, D.; Dho, J.; Blamire, M.G.; MacManus-Driscoll, J.L. High-resolution X-ray diffraction and transmission electron microscopy of multiferroic $BiFeO_3$ films. *Appl. Phys. Lett.* **2005**, *86*, 071913. [CrossRef]

38. Li, X.A.; Wang, X.W.; Li, Y.T.; Mao, W.W.; Li, P.; Yang, T.; Yang, J.P. Structural, morphological and multiferroic properties of Pr and Co co-substituted $BiFeO_3$ nanoparticles. *Mater. Lett.* **2013**, *90*, 152–155. [CrossRef]

39. Singh, M.K.; Jang, H.M.; Ryu, S.; Jo, M.H. Polarized Raman scattering of multiferroic $BiFeO_3$ epitaxial films with rhombohedral R3c symmetry. *Appl. Phys. Lett.* **2006**, *88*, 042907. [CrossRef]

40. Martín-Carrón, L.; de Andrés, A.; Martínez-Lope, M.J.; Casais, M.T.; Alonso, J.A. Raman phonons as a probe of disorder, fluctuations, and local structure in doped and undoped orthorhombic and rhombohedral manganites. *Phys. Rev. B* **2002**, *66*, 174303. [CrossRef]

41. Lobo, R.P.S.M.; Moreira, R.L.; Lebeugle, D.; Colson, D. Infrared phonon dynamics of a multiferroic $BiFeO_3$ single crystal. *Phys. Rev. B* **2007**, *76*, 172105. [CrossRef]

42. Pattanayak, S.; Choudhary, R.N.P. Synthesis, electrical and magnetic characteristics of Nd-modified $BiFeO_3$. *Ceram. Int.* **2015**, *41*, 9403–9410. [CrossRef]

43. Gu, Y.H.; Wang, Y.; Chen, F.; Chan, H.L.W.; Chen, W.P. Nonstoichiometric $BiFe_{0.9}Ti_{0.05}O_3$ multiferroic ceramics with ultrahigh electrical resistivity. *J. Appl. Phys.* **2010**, *108*, 094112. [CrossRef]

44. Dong, G.H.; Tan, G.Q.; Luo, Y.Y.; Liu, W.L.; Ren, H.J.; Xia, A. Investigation of Tb-doping on structural transition and multiferroic properties of $BiFeO_3$ thin films. *Ceram. Int.* **2014**, *40*, 6413–6419. [CrossRef]

45. Choudhary, R.N.P.; Perez, K.; Bhattacharya, P.; Katiyar, R.S. Structural and dielectric properties of mechanochemically synthesized $BiFeO_3$-$Ba(Zr_{0.6}Ti_{0.4})O_3$ solid solutions. *Mater. Chem. Phys.* **2007**, *105*, 286–292. [CrossRef]

46. Kumar, M.; Yadav, K.L.; Varma, G.D. Large magnetization and weak polarization in sol-gel derived $BiFeO_3$ ceramics. *Mater. Lett.* **2008**, *62*, 1159–1161. [CrossRef]

47. Arlt, G.; Hennings, D.; de With, G. Dielectric properties of fine-grained barium titanate ceramics. *J. Appl. Phys.* **1985**, *58*, 1619–1625. [CrossRef]

48. Saxena, P.; Kumar, A.; Sharma, P.; Varshney, D. Improved dielectric and ferroelectric properties of dual-site substituted rhombohedral structured $BiFeO_3$ multiferroics. *J. Alloys Compd.* **2016**, *682*, 418–423. [CrossRef]

49. Gao, Z.; Luo, Y.; Lyu, S.; Cheng, Y.; Zheng, Y.; Zhong, Q.; Zhang, W.; Lyu, H. Identification of Ferroelectricity in a Capacitor With Ultra-Thin (1.5-nm) $Hf_{0.5}Zr_{0.5}O_2$ Film. *IEEE Electr. Device Lett.* **2021**, *42*, 1303–1306. [CrossRef]

50. Tsymbal, E.Y.; Kohlstedt, H. Applied physics—Tunneling across a ferroelectric. *Science* **2006**, *313*, 181–183. [CrossRef]

51. Wen, Z.; Li, C.; Wu, D.; Li, A.; Ming, N. Ferroelectric-field-effect-enhanced electroresistance in metal/ferroelectric/semiconductor tunnel junctions. *Nat. Mater.* **2013**, *12*, 617–621. [CrossRef] [PubMed]

52. Kabelac, J.; Ghosh, S.; Dobal, P.; Katiyar, R. rf oxygen plasma assisted molecular beam epitaxy growth of $BiFeO_3$ thin films on $SrTiO_3$ (001). *J. Vac. Sci. Technol. B* **2007**, *25*, 1049–1052. [CrossRef]

53. Singh, S.K.; Kim, Y.K.; Funakubo, H.; Ishiwara, H. Epitaxial $BiFeO_3$ thin films fabricated by chemical solution deposition. *Appl. Phys. Lett.* **2006**, *88*, 162904. [CrossRef]

54. Bark, C.W.; Sharma, P.; Wang, Y.; Baek, S.H.; Lee, S.; Ryu, S.; Folkman, C.M.; Paudel, T.R.; Kumar, A.; Kalinin, S.V.; et al. Switchable Induced Polarization in $LaAlO_3$/$SrTiO_3$ Heterostructures. *Nano Lett.* **2012**, *12*, 1765–1771. [CrossRef]

55. Strelcov, E.; Kim, Y.; Yang, J.C.; Chu, Y.H.; Yu, P.; Lu, X.; Jesse, S.; Kalinin, S.V. Role of measurement voltage on hysteresis loop shape in Piezoresponse Force Microscopy. *Appl. Phys. Lett.* **2012**, *101*, 192902. [CrossRef]

56. Yuan, G.L.; Or, S.W.; Liu, J.M.; Liu, Z.G. Structural transformation and ferroelectromagnetic behavior in single-phase $Bi_{1-x}Nd_xFeO_3$ multiferroic ceramics. *Appl. Phys. Lett.* **2006**, *89*, 052905. [CrossRef]

57. Chu, Y.H.; Zhan, Q.; Yang, C.H.; Cruz, M.P.; Martin, L.W.; Zhao, T.; Yu, P.; Ramesh, R.; Joseph, P.T.; Lin, I.N.; et al. Low voltage performance of epitaxial $BiFeO_3$ films on Si substrates through lanthanum substitution. *Appl. Phys. Lett.* **2008**, *92*, 102909. [CrossRef]

58. Cai, W.; Fu, C.L.; Gao, R.L.; Jiang, W.H.; Deng, X.L.; Chen, G. Photovoltaic enhancement based on improvement of ferroelectric property and band gap in Ti-doped bismuth ferrite thin films. *J. Alloys Compd.* **2014**, *617*, 240–246. [CrossRef]

59. Wang, C.Y.; Liu, X.Y.; Sheng, S.; Zhou, Y.; Liu, H.R.; Sun, Y.X. Photovoltaic mechanism in Na-substituted $BiFeO_3$ films. *J. Phys. D Appl. Phys.* **2014**, *47*, 355104. [CrossRef]

60. Guo, Y.P.; Guo, B.; Dong, W.; Li, H.; Liu, H.Z. Evidence for oxygen vacancy or ferroelectric polarization induced switchable diode and photovoltaic effects in $BiFeO_3$ based thin films. *Nanotechnology* **2013**, *24*, 275201. [CrossRef]

61. Fan, Z.; Ji, W.; Li, T.; Xiao, J.X.; Yang, P.; Ong, K.P.; Zeng, K.Y.; Yao, K.; Wang, J. Enhanced photovoltaic effects and switchable conduction behavior in $BiFe_{0.6}Sc_{0.4}O_3$ thin films. *Acta Mater.* **2015**, *88*, 83–90. [CrossRef]

62. Gupta, S.; Tomar, M.; Gupta, V. Ferroelectric photovoltaic response to structural transformations in doped $BiFeO_3$ derivative thin films. *Mater. Des.* **2016**, *105*, 296–300. [CrossRef]

63. Peng, Z.W.; Wang, Y.L.; Liu, B.T. Enhanced open circuit voltage in photovoltaic effect of polycrystalline La and Ni co-doped $BiFeO_3$ film. *Funct. Mater. Lett.* **2015**, *8*, 1550002. [CrossRef]

64. Ukai, Y.; Yamazaki, S.; Kawae, T.; Morimoto, A. Polarization-Induced Photovoltaic Effects in Nd-Doped $BiFeO_3$ Ferroelectric Thin Films. *Jpn. J. Appl. Phys.* **2012**, *51*, 09LE10. [CrossRef]